Internal electric field construction on dual oxygen group-doped carbon nitride for enhanced photodegradation of pollutants under visible light irradiation

Fan Li[a,c], Muen Han[b], Yang Jin[d], Lili Zhang[a], Tong Li[b], Yaowen Gao[b], Chun Hu[b,*]

[a] *Key Laboratory of Drinking Water Science and Technology, Research Center for Eco-Environmental Sciences, Chinese Academy of Sciences, Beijing, 100085, China*
[b] *Key Laboratory for Water Quality and Conservation of the Pearl River Delta, Ministry of Education, Institute of Environmental Research at Greater Bay, Guangzhou University, Guangzhou, 510006, China*
[c] *University of Chinese Academy of Sciences, Beijing, 100049, China*
[d] *School of Space and Environment, Beihang University, Beijing, 102206, China*

ARTICLE INFO

ABSTRACT

Graphitic carbon nitride (g-C_3N_4), as metal-free and visible-light-driven photocatalyst, has been a promising alternative to replace the traditional inorganic photocatalyst. Herein, a dual oxygen group (C-O-C and C $=$ O) doped carbon nitride (ACN*) was prepared by a two-step thermal treatment process. The photocatalyst showed high and stable photocatalytic activity for the degradation and mineralization of refractory organic pollutants under visible light irradiation, as demonstrated with bisphenol A, phenol, 2-chlorphenol and diphenhydramine. By electron paramagnetic resonance spectroscopy and density functional theory calculations, higher valence-electron densities were formed around the O atoms of C-O-C and C $=$ O groups than around C and N atoms, constructing an internal electric field in ACN*, which was enhanced by light irradiation and the adsorption of pollutants by hydrogen bond and π-π bond interactions. Correspondingly, transfer processes of photogenerated carriers were proposed based on all experimental information obtained for pollutant photodegradation, including transfer of photoexcited electrons to the region around O atoms in the two types of oxygen groups, reaction with O_2 to form •O- 2, and donation of electrons from adsorbed pollutants to electron-poor tri-s-triazine motifs in ACN*. The synergetic oxidation by the two processes contributed to higher photodegradation of pollutants. This correlation between the transfer of photogenerated carries and pollutant degradation shed a new light on the construction of internal electric field in carbon nitride photocatalysis.

1. Introduction

An increasing number of refractory organic pollutants from the pharmaceutical, dyestuff, pesticide, paper and plastics industries are widely observed in natural and treated water[1], which is extremely harmful to the ecological environment and human health even at very low concentrations. However, traditional water treatment technologies are gradually becoming unable to meet the requirements for efficient water purification.[2] Nowadays, advanced oxidation processes (AOPs) has been becoming a promising technology for the degradation of contaminants using highly oxidizing free radicals. However, some compounding process of AOPs, such as UV/O_3, O_3/H_2O_2 and UV/H_2O_2, limit by harsh reaction conditions, complicated opertions and high costs [3]. Fortunately, photocatalysis, in which inexhaustible and clean solar energy can be harvested as a potential resource, has been regarded as an efficient and environmentally friendly wastewater treatment technique [4].

Recently, graphitic carbon nitride (g-C_3N_4), as a metal-free organic semiconductor, has emerged as an attractive visible-light photocatalyst due to its unique properties including nontoxicity, abundance, suitable band structure alignment and chemical stability [5]. Moreover, the position of CB and VB of g-C_3N_4 is located at about -1.3 and 1.4 V vs NHE, which is beneficial for the generation of •O- 2 and the direct oxidation of contaminants by h$^+$ [6]. However, its application is seriously limited by low surface area, restricted visible-light harvesting capacity and high charge recombination [7]. Hence, various strategies, such as bulk exfoliation to nanosheets [8], doping with elements/molecules [9,10], morphology design [11] and coupling with other metals/semiconductors [12,13] have been pursued to optimize its photocatalytic performance.

Among these modification approaches, exfoliating g-C$_3$N$_4$ from the bulk to form nanosheets has shown many advantages, such as enlarging the surface area to increase the number of reactive sites and reducing the transfer distance of photo-generated h$^+$/e-. Nevertheless, a fatal drawback of g-C$_3$N$_4$ nanosheets is the larger bandgap due to the strong quantum confinement effect, which shifts the conduction and valence band positions in opposite directions [8], severely limiting the visible light absorption.

Doping with non-metals is an efficient approach to extending the light response region. Recently, some researchers have reported that O-doped g-C$_3$N$_4$ exhibited enhanced visible-light photocatalytic activity. For instance, Li et al. [14] reported that O-doped g-C$_3$N$_4$, prepared by a H$_2$O$_2$ hydrothermal procedure, exhibited superior photoactivity towards MB degradation and H$_2$ evolution. Yu et al. [15] grafted hydroxyls (-OH) on g-C$_3$N$_4$ and achieved a ˜11-fold enhancement in H$_2$ generation. Meanwhile, in our previous research [1], it was found that doping with different elements can affect the charge distribution within the structure, and the uneven distribution of charges facilitates the formation of an internal electric field. The most common way to build an internal electric field is to form a heterojunction by matching g-C$_3$N$_4$ with other semiconductors. An et al. reported a novel graphitic carbon nitride (g-C$_3$N$_4$)/TiO2 hybrid photocatalyst achieving degradation and completely mineralization of contaminants and inactivation of Escherichia coli [16,17]. However, the formation of heterojunctions is affected significantly by the crystal structure, surface/interface properties and other features, which may result in high charge recombination. Liu et al. constructed a p-n homojunction for g-C$_3$N$_4$ by the implantation of -C≡N functional groups, which could induce a built-in electric field. Thus, the resulting homojunction structure overcomes the shortcomings of a heterojunction structure, and is highly efficient in charge separation and transfer, resulting in five-fold enhanced photocatalytic H$_2$ evolution activity [18]. Doping with non-metals (e.g. O, S and P) [9,19,20] often causes uneven distribution of charge, and facilitates the formation of an internal electric field, which is similar to the built-in electric field in a homojunction. Based on the above research, it should be possible to achieve a superior photocatalytic degradation effect, if a carbon nitride can be prepared having both oxygen doping characteristics and a porous nanosheet structure.

As for heterogeneous reaction, the pollutant-catalyst interaction plays a vital role, which had been neglected in many photocatalytic works previously. Recently, our research [2] has revealed that the interaction between pollutants and catalyst could promote the separation and transfer of photogenerated carriers at the interface for the effective degradation of pollutants. As a flexible 2D layered material, graphitic carbon nitride (g-C$_3$N$_4$) can provide an ideal surface for the adsorption of pollutant molecules, avoiding the effects of steric hindrance effectively [21]. Meanwhile, the layered conjugated structure of g-C$_3$N$_4$ may provide the needed adsorption sites [22]. In addition, because of the heteroatom doping, g-C$_3$N$_4$ can also introduce new adsorption sites, which will provide more possibilities for interaction between pollutants and catalyst at the interface.

Herein, we report synthesis of a nanostructured O-doped g-C$_3$N$_4$ (ACN*) with C-O-C and C = O groups by a combination of O doping and tailoring in dilute oxygen conditions, which created an internal electric field between O and the tri-s-triazine motifs, and achieved remarkably enhanced visible-light photocatalytic performance for pollutant degradation compared to bulk g-C$_3$N$_4$ (˜26.5 fold). This impressive improvement is mainly due to the construction of an internal electric field and strong interactions between the photocatalyst and pollutant, which greatly enhances the separation and transfer of photo-generated e-/h$^+$. Furthermore, the construction of an internal electric field and possible interaction modes for bisphenol A (BPA) and ACN* were identified by FTIR, transient photocurrent response and density functional theory (DFT) calculations. Thus, a possible electron transfer pathway is proposed for enhanced pollutant photodegradation.

2. Experimental Section

2.1. Preparation of ACN

ACN was prepared as follows. 20 g urea was mixed with different amounts of ammonium acetate (CH$_3$COONH$_4$) by thorough grinding for 20 min. The resultant solid mixtures were placed into a 200 mL porcelain crucible with a cover and calcined at 550 °C for 4 h with a heating rate of 5 °C/min in a muffle furnace. The obtained samples were designated as ACN-x (where x is the weight ratio of ammonium acetate to urea, x = 2.5%, 5%, 10%, 20%, respectively). In addition, bulk g-C$_3$N$_4$ (CN) was prepared by directly heating urea (20 g) without adding ammonium acetate according to a previous report [1].

2.2. Preparation of ACN*

ACN* was prepared by post-treatment of ACN. The prepared ACN-5% powder was moved to a porcelain crucible covered by aluminum foil and heated to 550 °C for 2 h with a ramping rate of 5 °C in a muffle furnace. CN* was prepared by the same post-treatment as ACN*.

2.3. Degradation Procedures

The photocatalytic activity of the prepared samples was evaluated by the degradation of bisphenol A (BPA), phenol, 2-chlorphenol (2-CP) and diphenhydramine (DP) (10 mg L^{-1}) under a LED lamp (PCX50C Discover reaction system, Beijing Perfectlight Co. Ltd. λ = 420-780 nm, light intensity = 100 mW·cm^{-2}). Prior to irradiation, the suspension was stirred in the dark for 30 min to achieve adsorption-desorption equilibrium. At certain time intervals, 1 ml of the suspension was withdrawn and then filtered with a 0.45 μm membrane. The concentration of BPA was measured by high-performance liquid chromatography (HPLC, 1200 series; Agilent) with a Zorbax SB-Aq column (5 μm, 4.6 × 250 mm; Agilent). PLS-SXE300/300UV was used as the Xenon light source. In the recycling experiment, the sample was filtered and washed with deionized water, and the recycled sample was dried at room temperature for the next cycle.

2.4. Characterization

Structural and morphological characterization of the samples was carried out using a field emission scanning electron microscope (FESEM, Hitachi, SU8020). High-resolution transmission electron microscopy (HRTEM) images were obtained using a JEM-2100 F TEM with an accelerating voltage of 200 kV. The Brunauer-Emmett-Teller (BET) surface area and pore size distribution of the samples were obtained by the BET equation and Barrett-Joyner-Halenda (BJH) method using a physisorption analyzer (ASAP 2020 HD88). Powder X-ray diffraction (XRD) patterns of the prepared samples were measured on a Scintag-xds-2000 diffractometer using Cu Kα radiation (λ = 1.540598 Å). Fourier transform infrared (FTIR) spectra were measured on a Nicolet 8700 FTIR spectrophotometer. UV-vis diffuse reflectance spectra (DRS) were determined via a Shimadzu U3900 recording spectrophotometer using Al$_2$O$_3$ as the reference. The photoluminescence (PL) intensities were obtained on a CARY ECLIPSE fluorescence spectrophotometer with an excitation wavelength of 350 nm. The transient photocurrent response plots and the EIS Nyquist analysis were obtained using an electrochemical system (CHI 660D electrochemical workstation) with a three-electrode quartz cell under a 150 W Xe lamp with a 420 nm cutoff filter. A platinum wire and saturated calomel electrode (SCE) were employed as the counter and reference electrodes. Electron spin resonance (ESR) measurements were collected by a using a Bruker model ESP 300E electron paramagnetic resonance spectrometer. X-ray photoelectron spectroscopy (XPS) measurements were performed via an AXIS-Ultra instrument using monochromatic Al Kα radiation (225 W, 15 mA, 15 kV).

2.5. Calculation Method and Model

The Vienna Ab Initio Simulation Package (VASP) [23,24] was used in this work for all the spin-polarized DFT calculations within the generalized gradient approximation (GGA) using the PBE functional formulation[25]. Projected augmented wave (PAW) [26] pseudopotentials were employed to describe the interactions between ionic cores and valence electrons. 1 (H), 4 (C), 5 (N), and 6 (O) valence electrons were explicitly taken into account. Valence-electron density color-filed maps were obtain with VESTA program [27,28].

The formation energies of CN to ACN (E_{form}(ACN)) and ACN to ACN* (E_{form} (ACN*)) were calculated as $E_{form}(ACN) = E(ACN) + 1/2 E(N_2) - E(CN) - 1/2 E(O_2)$ and $E_{form}(ACN*) = E(ACN*) + 1/2 E(N_2) - E(ACN) - E(O_2)$, respectively, where E(CN), E(ACN), and E(ACN*) are the total energies of the g-C_3N_4 sheet, ACN and ACN* sheet, $E(N_2)$ and $E(O_2)$ is the energy of the N_2 and O_2 in vacuum. From the above definition, a negative formation energy indicates that the reaction is exothermic and that the reaction is inclined to occur.

The adsorption energy, E_{ads}, of bisphenol A (BPA) on the g-C_3N_4 sheet was calculated as $E_{ads} = E_{BPA/surf} - E_{surf} - E_{BPA}$, where $E_{BPA/surf}$ and E_{surf} are the total energy of the g-C_3N_4 sheet with and without the BPA, respectively, and E_{BPA} is the energy of the bisphenol A molecule in vacuum. Based on the above definition, a negative E_{ads} indicates that the adsorption is exothermic and that the adsorbent–BPA system is stable.

3. Results and Discussion

3.1. Morphology and Structure

ACN* was synthesized by a two-step thermal treatment process involving thermal polymerization of urea and ammonium acetate, and second thermal treatment as illustrated in Scheme 1. First, urea and ammonium acetate linked with each other via acid-base interactions [29]. The mixture was calcined under air to form carbon nitride with C-O-C groups (ACN). Second, the prepared ACN-5% powder was moved to a porcelain crucible covered by aluminum foil and further calcined in a muffle furnace to obtain ACN*. In this process, ACN reacted with oxygen at high temperature and part of ACN was decomposed into a series of gases (CO_2, NO_2 etc.), which generated a large amount of pores and, the bulk structure was successfully exfoliated. Meanwhile, C = O was further introduced into the tri-s- triazine motifs.

Field emission scanning electron microscope (FESEM) images (Fig. 1a, c) show that CN and ACN both exhibit an irregular stacked interlayer-like structure, which is the typical morphology according to previous reports. Compared to CN and ACN, ACN* (Fig. 1d) presents thinner fragmentized nanosheets with curled and rough edges as a result of minimizing the surface energy [30]. Transmission electron microscope (TEM) images (Fig. 1e, g and h) further show that ACN* is thinner and contains many pores. The ultrathin nanosheets and pores can expose more active sites and improve the charge mobility in both the vertical and in-plane directions [31]. Interestingly, CN* exhibits a
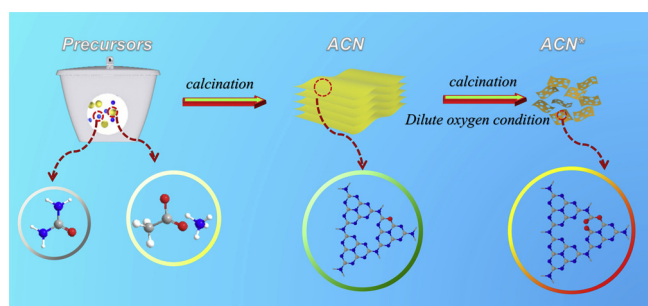
Scheme 1. Schematic illustration of preparation for ACN*.

thicker sheet structure and fewer pores (Fig. 1b, f), which indicates that the first step of thermal polymerization with ammonium acetate (CH_3COONH_4) facilitates the exfoliation of bulk g-C_3N_4 and the generation of pores in the second thermal treatment step. Furthermore, the BET specific surface areas of CN and ACN are 45.4 and 41.3 $m^2 g^{-1}$, and the BET specific surface areas of CN* and ACN* increased to 92.2 and 204.7 $m^2 g^{-1}$ through the second thermal treatment step (Fig. 2a). Meanwhile, all the samples show type IV isotherms and type H3 hysteresis loops, indicating the existence of mesopores [32]. These are all consistent with the analysis of SEM and TEM results (Fig. 1).

The powder XRD patterns of the prepared samples are shown in Fig. 2b. The XRD pattern for CN mainly shows two characteristic peaks at 13.0° and 27.4°, which can be assigned to the (100) and (002) crystal planes of pristine g-C_3N_4, representing the in-plane structural packing of tri-s-triazine motifs and the periodic stacking of layers of conjugated aromatic systems, respectively [5]. After copolymerization with ammonium acetate, the diffraction peak position of (002) for ACN shifts to a lower angle, implying the increase of the interlayer distance, attributed to the larger radius of the doped O atom than that of the replaced N atom [33]. When ACN was further calcined, the peak position of (002) shifted to higher angle, indicating a smaller stacking distance between inner layer of nanosheets [8]. In addition, the (100) peak for ACN* broadened and weakened, suggesting that the second thermal treatment step causes a decrease in the in-planar layer dimension [20]. Similar changes also occur on CN*. Therefore, ACN* exhibits a loose interlayer structure and denser in-plane structure due to the two-step treatment.

Fig. 2c shows the FTIR patterns of CN, CN*, ACN and ACN*. The FTIR peak for CN at 812 cm^{-1} corresponds to the breathing mode of heptazine units and the peaks at 1200-1600 cm^{-1} are typical stretching vibration modes of C = N and C-N heterocycles [18]. It can be seen that the main peaks of CN*, ACN and ACN* are very similar to those of CN, confirming that the general structure of g-C_3N_4 is preserved. However, due to the low quantity of O, the C-O and C = O peaks may be overlapped by aromatic C-N stretching bands in ACN and ACN* [34]. It was noteworthy that the FTIR peaks at 1238 and 1407 cm^{-1}, which can be attributed to the = C (sp^2) bending vibration and out-of-phase stretching vibration of N-C (sp^3), shifted by 8-10 cm^{-1} toward higher frequencies after O-doping. This may be due to the effect of the higher electronegativity of O atoms on the adjacent C-N [14]. In addition, the intensity of peaks at 810, 1208, 1335 and 1541 cm^{-1} significantly weakens and even disappears after the two-step treatment, suggesting that the s-triazine ring system is partly destroyed due to the two-step treatment [34].

The optical absorption properties of g-C_3N_4 characterized by UV-vis diffuse reflectance spectra (Fig. 2d). Compared with CN, the adsorption edge of ACN and ACN* exhibits a red-shift from 460 to 520 and 600 nm, which corresponds to the change of color for the materials. In general, g-C_3N_4 nanosheets shows an obvious blue shift of the intrinsic absorption edge[8]. However, the adsorption edge of CN* do not be narrowed, suggesting that oxygen doping significant changes the band structure and compensates for the band gap broadening caused by the nanosheets structure. Moreover, it can be observed that ACN* and CN* exhibit a broader and stronger Urbach tail, which can be attributed to the multiple reflection of incident light within the porous architecture [30]. Meanwhile, the band gap energies of the samples was obtained via the transformed Kubelka-Munk function. It can be seen from that the bandgap energies of CN, CN*, ACN and ACN* is determined to be 2.84, 2.84, 2.73 and 2.46 eV, respectively (Fig. S1a). And the energy band positions of the as-prepared samples are shown in Fig. S1c, which in favor of the visible-light absorption and the separation of photogenerated h^+/e-.

3.2. Construction of Internal Electric Field

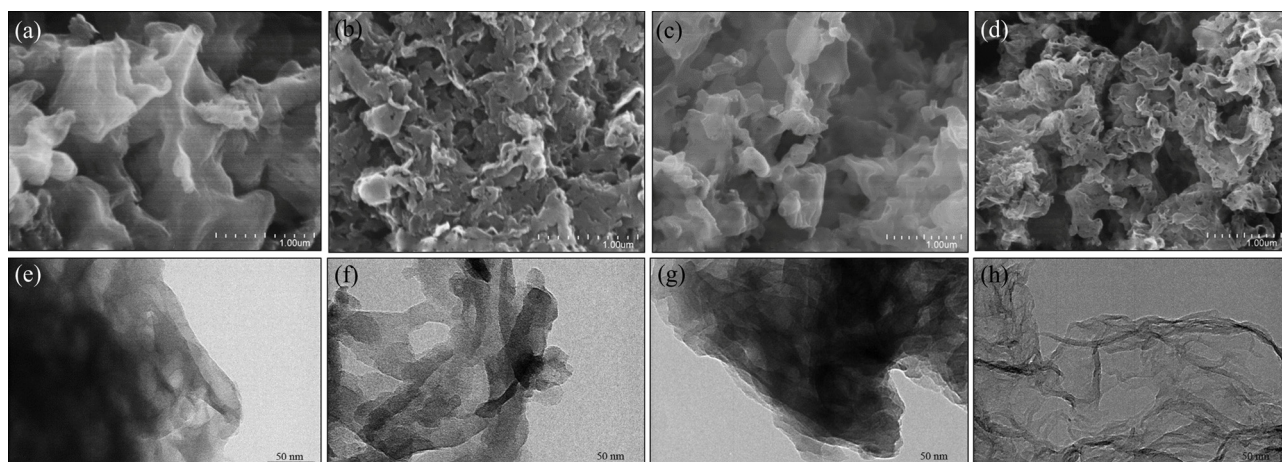Organic elemental analysis (OEA) was used to analyze the elemental

Fig. 1. FESEM images of (a) CN, (b) CN*, (c) ACN and (d) ACN*; HRTEM images of (e) CN, (f) CN*, (g) ACN and (h) ACN*.
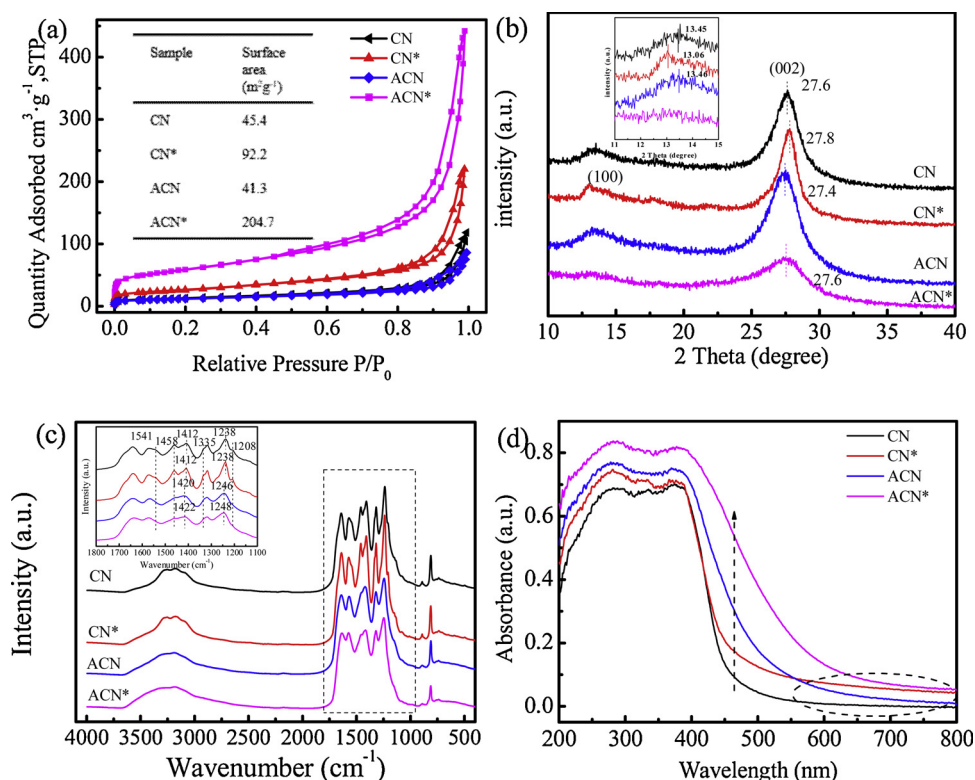

Fig. 2. (a) N$_2$ adsorption-desorption isotherms, (b) XRD patterns, (c) FTIR spectra and (d) UV-vis diffuse reflectance spectras of CN, CN*, ACN and ACN*.

Table 1
Results of organic elemental analyses.

samples	C (Atomic %)	N (Atomic %)	H (Atomic %)	O (Atomic %)
CN	34.19	60.30	1.62	3.89
ACN	34.84	58.49	1.66	5.01
ACN*	35.81	54.18	1.58	8.43

content of the samples (Table 1). The O contents of CN, ACN and ACN* were determined to be 4.07, 5.01 and 8.43%, suggesting that both steps in the two-step treatment can increase the doping of O element. In addition, the N content decreased from 60.30% to 54.18%, indicating that O atoms may be doped into the carbon nitride skeleton by substituting for N atoms. The elemental valence state in the samples was analyzed by XPS (Fig. 3a). As compared to CN with two apparent peaks

at 288.3 and 284.8 eV (corresponding to N = C-N and reference carbon) [31], a new peak in the C 1s spectrum of ACN appears at 286.8 eV, which corresponds to C-O-C. The C 1s spectrum for ACN* contains another new peak located at 287.7 eV, corresponding to the C = O group [9]. These results suggest that C-O-C groups were introduced into ACN with the copolymerization of urea and ammonium acetate, and the C = O group was introduced into ACN* during the second thermal treatment step.

In order to further confirm the location of O atoms in the tri-s-triazine motifs of ACN and ACN*, Density Functional Theory (DFT) calculations were performed. First, the surface structure of carbon nitride was optimized, and the result shows that the potential energy of the corrugated surface is 6.65 eV lower than that of a planar surface in the 3 × 3 sheet (Fig. S2a and b), which indicates that the corrugated conformation is stable for g-C$_3$N$_4$. Then, based on this result, the specific doping site of the O atom in ACN was calculated by substituting
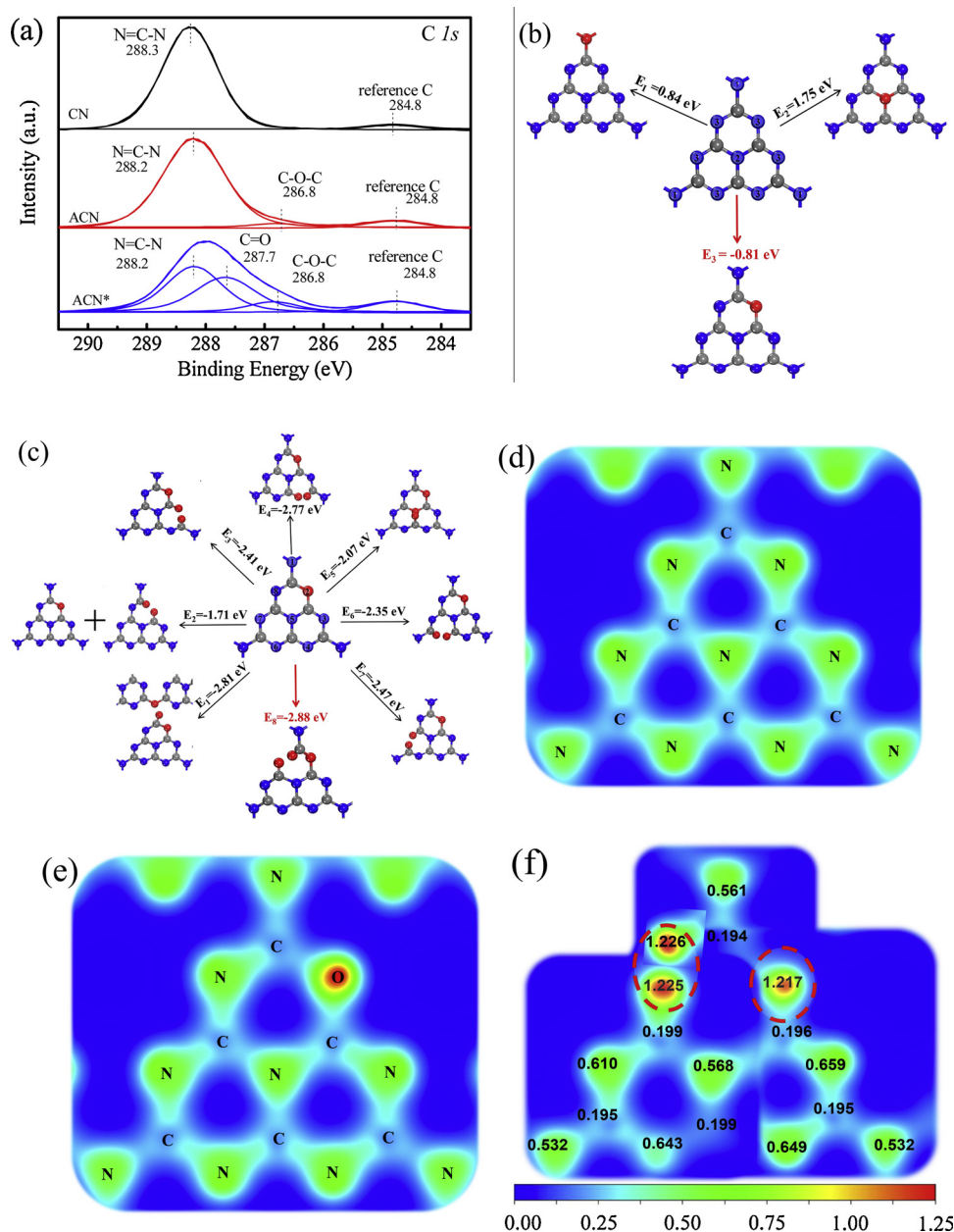
Fig. 3. (a) XPS C 1s spectra, calculated formation energy of (b) ACN from CN and (c) ACN* from ACN, the structure and two-dimensional valence-electron density color-filled maps of CN (d), ACN (e) and ACN* (f) (length unit Bohr).

the N with O at three different N sites (Fig. 3b). The formation energy (E) of O atoms substituted at N (site 1, 2 and 3) positions is 0.84, 1.75 and -0.81 eV, respectively, suggesting that the substitution at site 3 (edge N) is more favorable based on its lower formation energy [35]. Because the H content of ACN* shows no apparent increase (Table 1), there are eight possible doping sites in ACN (Fig. 3c). The calculation result shows that substitution site 8 is much more favorable than the other 7 positions. Considering that the electronegativity of O is higher than that of N, doping of O atoms by substituting for N atoms tends to alter the electronic structure of ACN and ACN*, which was characterized by two-dimensional valence-electron density color-filled maps. The largest electron density distribution region in ACN appears around the O atom compared with CN (Fig. 3d and e), and its maximum valence-electron density is as high as 1.218 e/Bohr^3. After further introducing C = O into ACN* (Fig. 3f), the valence-electron densities around the O atoms (C-O-C and C = O) are all significantly higher than those around C and N atoms. The apparent uneven distribution of electrons leads to

the formation of high- and low-density regions of valence electrons, that is, an internal electric field was constructed.

The presence of single electrons in the prepared samples was monitored by electron paramagnetic resonance (EPR) spectra. As shown in Fig. 4a, a single Lorentzian line centered at g = 2.0034 is observed for the four samples, suggesting the generation of unpaired electrons on π-conjugated carbon nitride aromatic rings. Compared with CN, ACN exhibits a significantly stronger ESR signal, suggesting a much higher concentration of unpaired electrons, which is beneficial for the photogeneration of active radical pairs [30]. However, the introduction of C = O groups results in a decrease in the ESR signal intensity of ACN* in comparison to that of ACN. These results can be explained by the doping location of C-O-C and C = O in the DFT calculation (Fig. 3b and c). Since an O atom has one more valence electron than a N atom, extra electrons would be produced and redistributed to the nearest C atoms and delocalized among the big π bonds of ACN due to the substitution of O atoms on N sites [36]. When introducing a
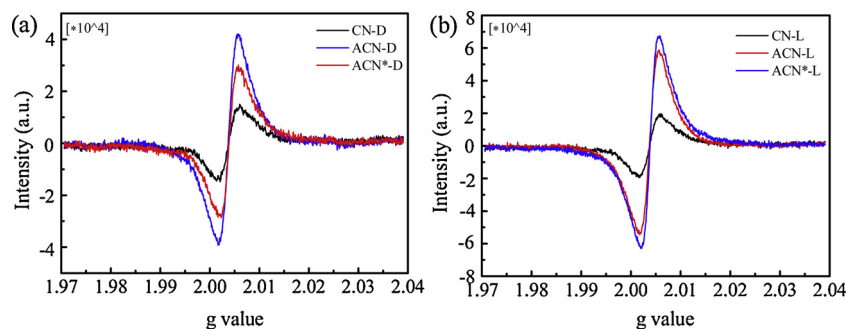
Fig. 4. EPR spectra of CN, ACN and ACN* under (a) dark condition, (b) visible-light condition. (D and L denote dark condition and visible-light condition).

C = O group into the basic unit containing C-O-C, the extra electrons in ACN* may pair with each other, which decreases the content of unpaired electrons and the EPR signal intensity. Notably, the EPR signal intensity is markedly enhanced when the samples are irradiated under visible light (Fig. 4b), indicating efficient photochemical generation of radical pairs in the samples [37]. Also, the EPR signal intensity of ACN* exhibits a greater degree of enhancement compared with that of ACN, and shows the highest EPR signal intensity, indicating that the consistency of the internal electric field and the photoexcited electric field causes the further polarization of the internal electric field.

The separation and recombination of photogenerated carries was characterized by PL spectra, transient photocurrent response and EIS Nyquist plots. Fig. 5a shows the PL spectra performed with an excitation wavelength of 350 nm. CN shows the highest PL peak intensity, suggesting that a high recombination efficiency of the charge carriers. After the introduction of C-O-C, the PL intensity of ACN is much lower than that of CN, implying that the O dopant does not serve as the recombination center of photogenerated e-/h$^+$. Notably, ACN* exhibits the lowest PL intensity, indicating that it has the lowest charge recombination rate [38], revealing that the introduction of C-O-C and C = O may play a synergistic role in charge separation and transfer. In

addition, CN* also shows a lower PL peak intensity than CN, indicating that the ultrathin thickness and pore structure also facilitates the separation of charge carriers. Moreover, the emission peaks of CN*, ACN and ACN* all display a red shift from 474 to 482, 500 and 510 nm, which is also consistent with the extension of the absorption edge toward longer wavelength (Fig. 2d). Fig. 5b shows the transient photocurrent responses of CN, CN*, ACN and ACN* under visible-light irradiation in six on-off cycles. It is clear to see that all samples exhibit a sensitive photocurrent response during on/off irradiation cycles under visible light. Among all the samples, ACN* exhibits the highest photocurrent response, which is nearly 2.5 times higher than that of CN, which is consistent with the trend seen in their photocatalytic performance. Meanwhile, the EIS analysis of the samples is shown in Fig. 5c. ACN* also shows the smallest diameter Nyquist circle, evidencing the greatly enhanced interfacial charge transfer efficiency [11]. The results of the three optical and photoelectric measurements all indicate that lower charge recombination and efficient separation and transfer occur in ACN*. This may be due to two aspects as follows: (1) the O atoms can act as trapping sites to inhibit the direct recombination of electrons and holes [39], and the internal electric field facilitates the separation and transfer of the photogenerated charges; (2) the ultrathin nanosheets and
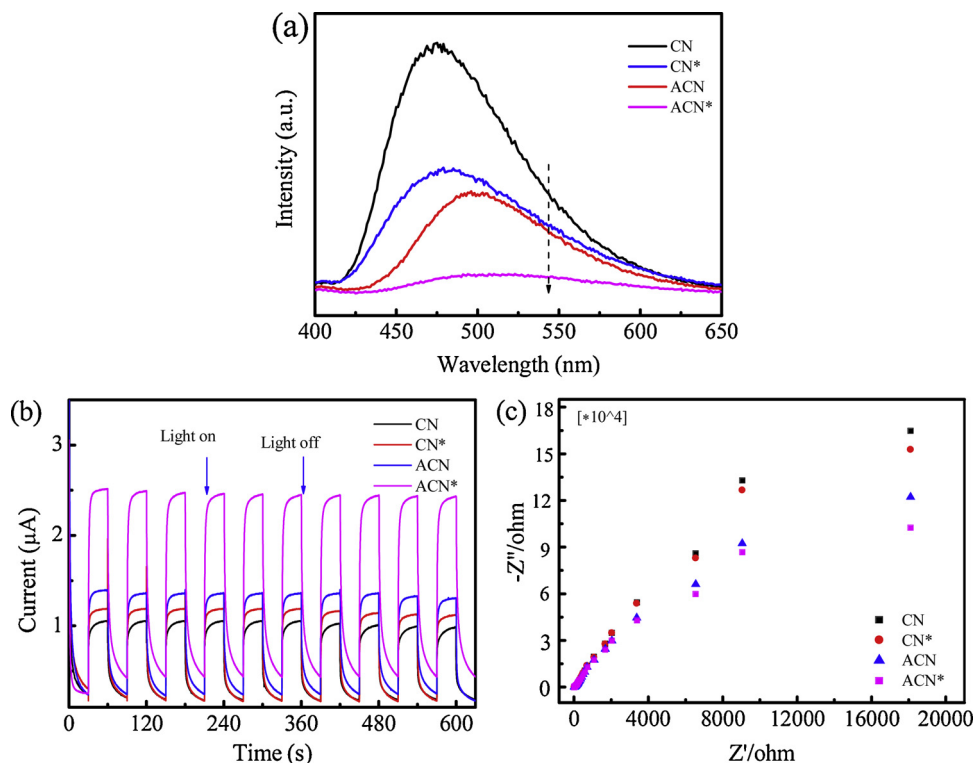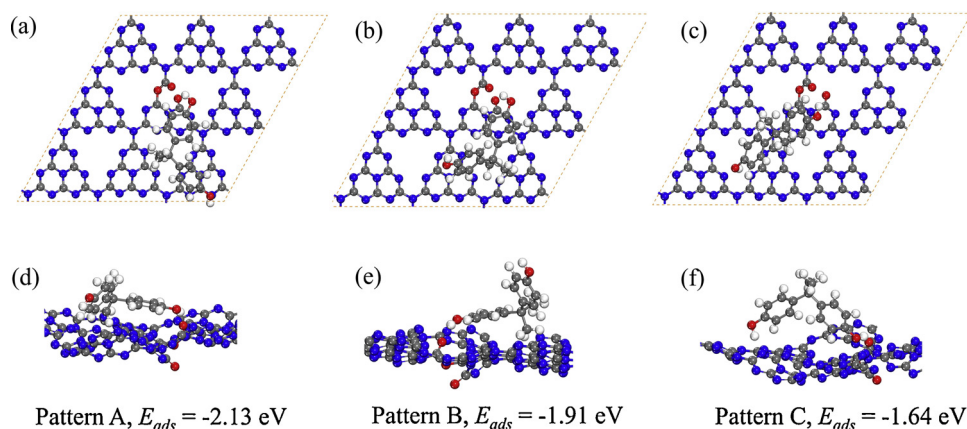

Fig. 5. (a) Photoluminescence (PL)spectra, (b) transient photocurrent responses and (c) EIS Nyquist plots of as-synthesized CN, CN*, ACN and ACN*.

Fig. 6. Optimized interaction patterns (top view and side view) and adsorption energies of BPA adsorbed on the corrugated ACN* surface (a and d for adsorption pattern A; b and e for pattern B; c and f for pattern C).

decreased in-plane dimension can shorten the diffusion length of photogenerated charges and facilitate the transfer of charges to the surface [31].

3.3. Interaction of Pollutants and ACN*

Fig. S3 shows the FTIR spectra of ACN* with different pollutants adsorbed, including BPA, phenol, 2-CP and DP (the adsorption amounts are 10.3%, 8.7%, 17.4% and 34.7%). In the FTIR spectra of ACN*, the peak at $3322 \, cm^{-1}$ is ascribed to the stretching vibration of OH [ν (OH)] [40]. After the pollutants are adsorbed on the surface of ACN*, the OH peak shifts to higher wavelength, indicating that an interaction occurs between the pollutants and ACN*.

To further understand the adsorption patterns between BPA and ACN*, the possible interaction models were calculated. Different from the adsorption pattern of CN and ACN (Fig. S4 and S5), hydrogen bonding occurs in the ACN* systems. For interaction patterns A and B (Fig. 6), two and one π-π interactions are formed, respectively. The π-π interactions between the electron rich ACN* and aromatic molecules is beneficial for activation of the molecules by promoting further charge transfer [21]. Moreover, a hydrogen bond between H atom in the OH group of BPA and O atom in carbonyl group of the ACN* surface forms, which further strengthen the interaction between BPA and ACN*, and the adsorption energy of pattern A and B is -2.13 and -1.91 eV, respectively. There is also another interaction model (pattern C), in which only a hydrogen bond forms between the BPA and the surface, which corresponds to an adsorption energy of -1.64 eV. Evidently, pattern A is the main adsorption pattern due to having the lowest adsorption energy, that is, hydrogen bonding and π-π interaction are the main adsorption modes.

Furthermore, the EPR signal of ACN* with different pollutants adsorbed was investigated. As shown in Fig. 7a, with the adsorption of different pollutants, the EPR signal intensity of ACN* was significantly strengthened in the dark in all cases. The adsorption of pollutants by hydrogen bonding and π-π interactions may contribute to the enhancement of the internal electric field, which facilitates the offset of the valence electrons to produce more unpaired electrons. Moreover, stronger EPR intensity was observed for ACN* with adsorbed pollutants under visible light irradiation (Fig. 7b). Meanwhile, the transient photocurrent responses of ACN* with different adsorbed pollutants all exhibit significant enhancement to different degrees (Fig. 7c). These results implied that ACN* with adsorbed pollutants can be excited to generate more unpaired electrons and promote more efficient separation and transfer of photogenerated e-/h$^+$ under visible light irradiation.

3.4. Photocatalytic Performance

Fig. 8 shows the photocatalytic degradation of BPA by the prepared samples. After introducing different amounts of O into g-C$_3$N$_4$, the photocatalytic activity towards BPA degradation noticeably increased in comparison with CN (Fig. 8a), which indicates that a suitable amount of C-O-C doping can effectively improve the visible-light catalytic activity of ACN. Furthermore, after the second thermal treatment step, the degradation rate of BPA in the ACN* suspension reaches 99% within 30 min, which is 31.38, 17.1 and 8.03 times higher than that in CN, CN* and ACN (Fig. 8b and c). Meanwhile, the TOC removal rate of BPA by ACN* is up to 72.79% within 60 min (Fig. 8d), which is greatly higher than that in the suspensions of CN (9.27%), CN* (33.50%) and ACN (44.95%). These results demonstrate that the internal electric field, formed by the introduction of two different types of oxygen functional groups (C-O-C and C = O), can remarkably improve the photocatalytic performance towards pollutant degradation by efficient photogenerated e-/h$^+$ separation and transfer. Moreover, the corresponding photocatalytic performance at different wavelength and Xenon light were also studied. As shown in Fig. S6a, the compete removal of BPA was finished within 20 min under Xenon light (λ > 420 nm), which is more efficient than that under LED white light (λ > 420 nm) with the same light intensity (100 mW·cm^{-2}). The result can be explained by that the spectrum distribution of Xenon light is much more broad than that of LED white light (Fig. S6b and c). It could also been that the photocatalytic activity was enhanced under λ = 365 and 420 nm and weaker under 520 and 630 nm than that under LED white light. However, even if the wavelength was increased to 530 nm and 630 nm, BPA could still be degraded to varying degrees, which was according to the UV-vis diffuse reflectance spectra of ACN* in Fig. 2b.

The stability of ACN* was tested after recycling the catalyst by filtration, washing and drying. As shown in Fig. 9a, there was no obvious deactivation of ACN* compared with the first photocatalytic reaction. After five cycles, BPA could still be completely degraded within 40 min. To further investigated the adaptability of ACN* for different organic pollutants, phenol, 2-CP and DP were used for degradation under the same conditions. As shown in Fig. 9b, the degradation rates of phenol, 2-CP and DP in the ACN* suspension reached 96.7%, 97.3% and 88.6% within 30 min and the corresponding TOC removal was 67.3%, 61.5% and 55.0% within 60 min (inset spectra of Fig. 9b), respectively. Hence, ACN* is an effective photocatalyst with good stability and adaptability.

3.5. Photocatalytic mechanism

In order to further understand the photocatalytic mechanism of ACN*, p-benzoquinone (p-BQ), tert-butyl alcohol (TBA) and Na$_2$C$_2$O$_4$ were used as scavengers for superoxide radicals (•O- 2), hydroxyl
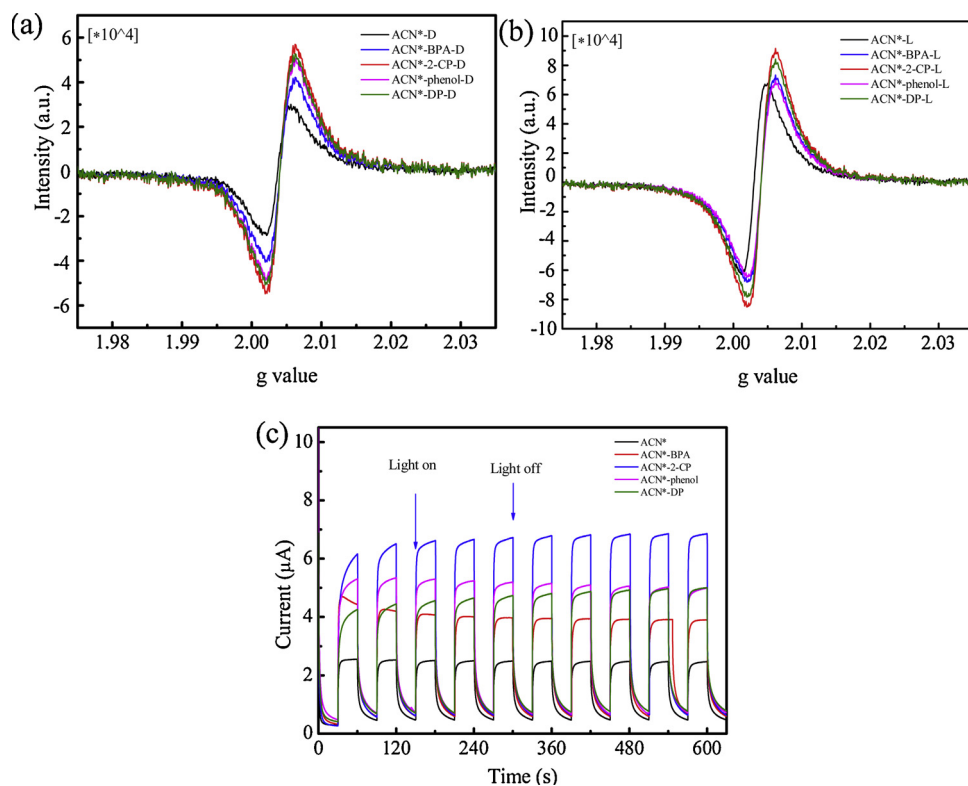
Fig. 7. EPR spectra of ACN* adsorbed different pollutants under (a) dark and (b) visible-light condition, and (c) transient photocurrent responses of ACN* adsorbed different pollutants. (D and L denote dark condition, visible-light condition).
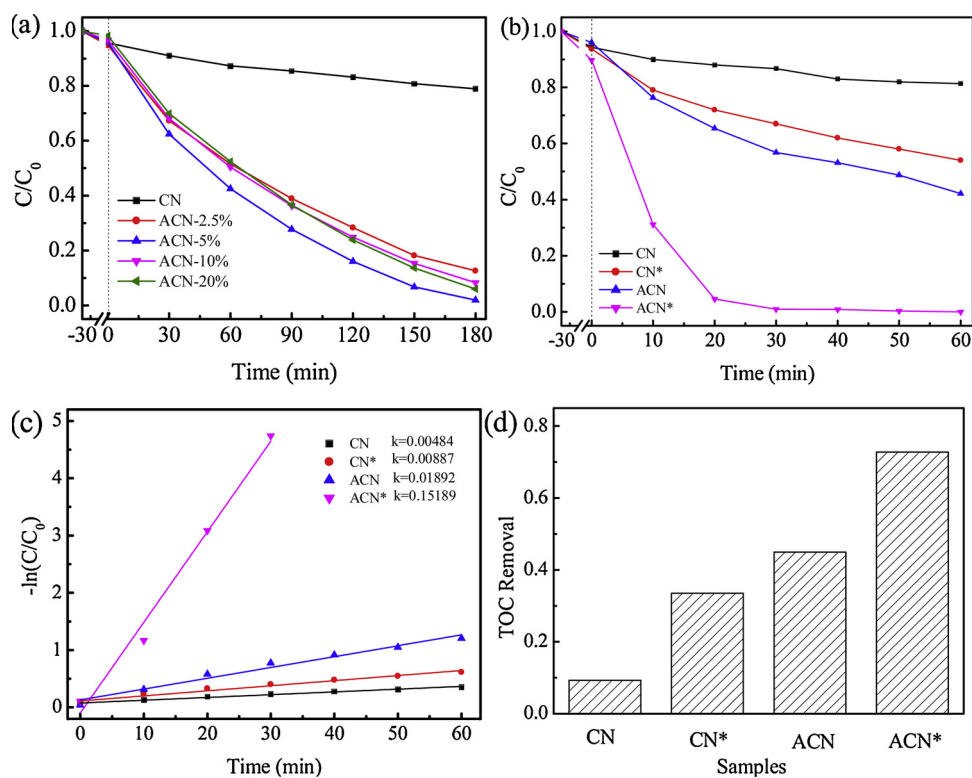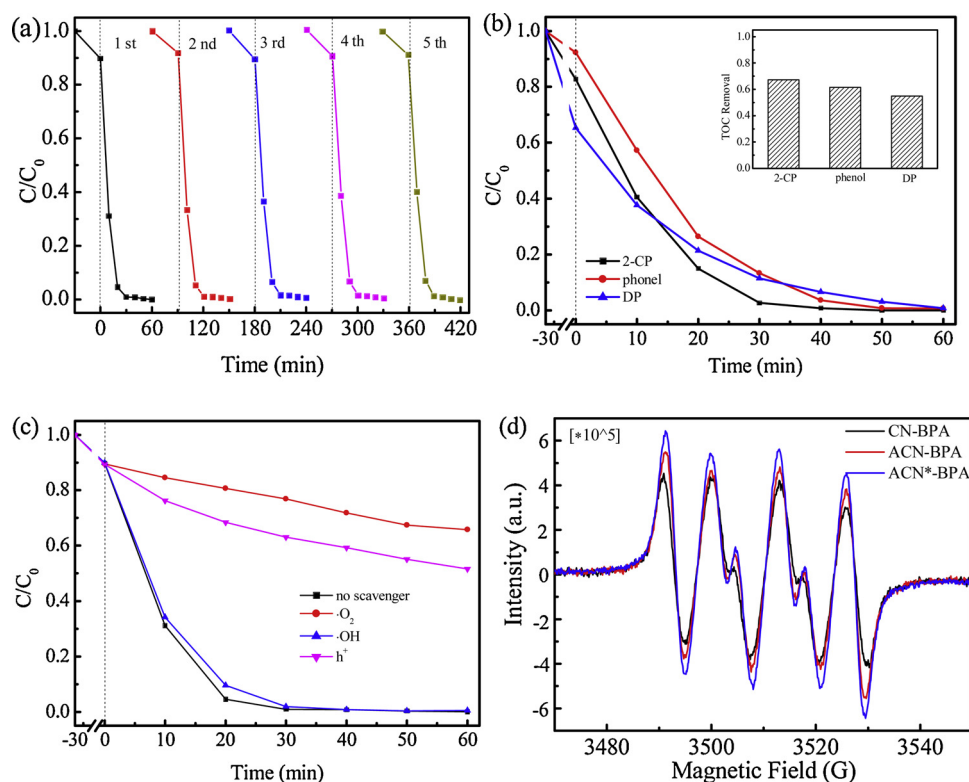

Fig. 8. (a) BPA degradation and experiments of CN and ACN-x, (b) BPA degradation experiments and (c) kinetic linear simulation curves (d) TOC removal of CN, CN*, ACN and ACN*. (BPA concentration: 10 ppm).

Fig. 9. (a) Cycling test, (b) decomposition curves of 2-CP, phenol and DP (the inset spectra is the TOC removal of ACN* for 2-CP, phenol and DP) (c) active species trapping experiments of ACN*, (d) BMPO spin-trapping EPR spectra for•O- 2. (Concentration of all pollutants is 10 ppm.).

radicals (•OH) and photoexcited pores (h$^+$), respectively [41–44]. As shown in Fig. 9c, the degradation rate obviously decreased when p-BQ and Na$_2$C$_2$O$_4$ were added, while negligible inhibition was observed on addition of TBA, suggesting that •OH does not contribute to BPA degradation. The results indicated that •O- 2 and h$^+$ are the main active species for BPA degradation. h$^+$ can only degrade pollutants adsorbed on the surface of the catalyst. Therefore, pollutant adsorption may greatly affect the degradation efficiency. The spectra of zeta potential as a function of pH for ACN* (Fig. S7a) shows that the surface of ACN* would become more positive with the decrease of pH, which would facilitate the adsorption of BPA. With pH decreasing from 12 to 3 (Fig. S7b), the adsorption amount of BPA increased from 4.6% to 24.6%, while the time to obtain complete removal of BPA was reduced from 60 min to 10 min. It could be seen that the more pollutant is adsorbed on ACN*, the better the degradation effect by h$^+$ should be; as one of the main active species, this determines that the interaction of ACN* and pollutants is critical to the degradation process. In addition, the generation of active species (•O- 2) over ACN* was probed by BMPO spin-trapping EPR spectra. To further simulate the true degradation, the samples after adsorption of BPA were measured for the •O- 2 intensity. As shown in Fig. 9d, with pollutant adsorption, more •O- 2 is generated in the suspension of ACN* than that in the suspension of CN and ACN. Considering the EPR analysis of ACN* with different pollutants adsorbed, the pollutant adsorption contributes to the enhancement of the internal electric field, remarkably improving the separation and transfer of photogenerated e-/h$^+$, which facilitates the oxidation process of h$^+$ and the generation of •O- 2.

In summary, the introduction of two types of oxygen functional groups (C-O-C and C = O) leads to polarization of the charge distribution, which constructs an internal electric field. The oxygen-containing zone is the negative pole and the tri-s-triazine motif is the positive pole. Meanwhile, pollutant adsorption can enhance the further polarization of the internal electric field by hydrogen bonding and π-π interaction between pollutants and ACN*. Based on these effects, a

cyclic transfer process of photogenerated carriers is proposed. The pollutant removal process is as follows in ACN* suspensions under visible-light irradiation. On the one hand, photoexcited electrons transfer to the dual oxygen groups and are trapped by O$_2$ to generate •O- 2 for degradation of pollutant in water. On the other hand, pollutants adsorbed on the surface of ACN* are decomposed by transferring electrons to the positive pole by hydrogen bonding and π-π interaction with ACN*. Thus, this work strongly calls attention to the internal electric field modification of photocatalysts and the interaction between pollutants and materials to realize environmental remediation.

4. Competing financial interest

The authors declare no competing financial interest.

Acknowledgments

Appendix A. Supplementary data

Supplementary material related to this article can be found, in the online version, at doi:https://doi.org/10.1016/j.apcatb.2019.05.007.

References

[1] L. Lyu, D. Yan, G. Yu, W. Cao, C. Hu, Efficient Destruction of Pollutants in Water by a Dual-Reaction-Center Fenton-like Process over Carbon Nitride Compounds-Complexed Cu(II)-CuAlO$_2$, Environ Sci. Technol. 52 (2018) 4294–4304.
[2] F. Li, L. Zhang, C. Hu, X. Xing, B. Yan, Y. Gao, L. Zhou, Enhanced azo dye decolorization through charge transmission by σ-Sb^{3+}-azo complexes on amorphous Sb$_2$S$_3$ under visible light irradiation, Applied Catalysis B: Environmental 240 (2019) 132–140.

[3] R. Li, M. Cai, Z. Xie, Q. Zhang, Y. Zeng, H. Liu, G. Liu, W. Lv, Construction of heterostructured $CuFe_2O_4$/g-C_3N_4 nanocomposite as an efficient visible light photocatalyst with peroxydisulfate for the organic oxidation, Applied Catalysis B: Environmental 244 (2019) 974–982.

[4] C. Pan, J. Xu, Y. Wang, D. Li, Y. Zhu, Dramatic Activity of C_3N_4/$BiPO_4$ Photocatalyst with Core/Shell Structure Formed by Self-Assembly, Advanced Functional Materials 22 (2012) 1518–1524.

[5] Q. Han, B. Wang, Y. Zhao, C. Hu, L. Qu, A Graphitic-C_3N_4 "Seaweed" Architecture for Enhanced Hydrogen Evolution, Angewandte Chemie 54 (2015) 11433–11437.

[6] Q. Zhang, P. Chen, C. Tan, T. Chen, M. Zhuo, Z. Xie, F. Wang, H. Liu, Z. Cai, G. Liu, W. Lv, A photocatalytic degradation strategy of PPCPs by a heptazine-based CN organic polymer (OCN) under visible light, Environmental Science: Nano 5 (2018) 2325–2336.

[7] W. Che, W. Cheng, T. Yao, F. Tang, W. Liu, H. Su, Y. Huang, Q. Liu, J. Liu, F. Hu, Z. Pan, Z. Sun, S. Wei, Fast Photoelectron Transfer in (Cring)-C_3N_4 Plane Heterostructural Nanosheets for Overall Water Splitting, J Am Chem Soc 139 (2017) 3021–3026.

[8] P. Niu, L. Zhang, G. Liu, H.-M. Cheng, Graphene-Like Carbon Nitride Nanosheets for Improved Photocatalytic Activities, Advanced Functional Materials 22 (2012) 4763–4770.

[9] H. Wang, S. Jiang, S. Chen, D. Li, X. Zhang, W. Shao, X. Sun, J. Xie, Z. Zhao, Q. Zhang, Y. Tian, Y. Xie, Enhanced Singlet Oxygen Generation in Oxidized Graphitic Carbon Nitride for Organic Synthesis, Advanced materials 28 (2016) 6940–6945.

[10] Y. Kofuji, Y. Isobe, Y. Shiraishi, H. Sakamoto, S. Tanaka, S. Ichikawa, T. Hirai, Carbon Nitride-Aromatic Diimide-Graphene Nanohybrids: Metal-Free Photocatalysts for Solar-to-Hydrogen Peroxide Energy Conversion with 0.2% Efficiency, J Am Chem Soc 138 (2016) 10019–10025.

[11] L. Cui, J. Song, A.F. McGuire, S. Kang, X. Fang, J. Wang, C. Yin, X. Li, Y. Wang, B. Cui, Constructing Highly Uniform Onion-Ring-like Graphitic Carbon Nitride for Efficient Visible-Light-Driven Photocatalytic Hydrogen Evolution, ACS Nano (2018).

[12] S. Ma, S. Zhan, Y. Jia, Q. Shi, Q. Zhou, Enhanced disinfection application of Ag-modified g-C_3N_4 composite under visible light, Applied Catalysis B: Environmental 186 (2016) 77–87.

[13] Y. Zheng, Z. Yu, H. Ou, A.M. Asiri, Y. Chen, X. Wang, Black Phosphorus and Polymeric Carbon Nitride Heterostructure for Photoinduced Molecular Oxygen Activation, Advanced Functional Materials 28 (2018).

[14] J. Li, B. Shen, Z. Hong, B. Lin, B. Gao, Y. Chen, A facile approach to synthesize novel oxygen-doped g-C_3N_4 with superior visible-light photoreactivity, Chem Commun (Camb) 48 (2012) 12017–12019.

[15] S. Yu, J. Li, Y. Zhang, M. Li, F. Dong, T. Zhang, H. Huang, Local spatial charge separation and proton activation induced by surface hydroxylation promoting photocatalytic hydrogen evolution of polymeric carbon nitride, Nano Energy 50 (2018) 383–392.

[16] G. Li, X. Nie, Y. Gao, T. An, Can environmental pharmaceuticals be photocatalytically degraded and completely mineralized in water using g-C_3N_4 /TiO_2 under visible light irradiation?—Implications of persistent toxic intermediates, Applied Catalysis B: Environmental 180 (2016) 726–732.

[17] G. Li, X. Nie, J. Chen, Q. Jiang, T. An, P.K. Wong, H. Zhang, H. Zhao, H. Yamashita, Enhanced visible-light-driven photocatalytic inactivation of Escherichia coli using g-C_3N_4/TiO_2 hybrid photocatalyst synthesized using a hydrothermal-calcination approach, Water Res 86 (2015) 17–24.

[18] G. Liu, G. Zhao, W. Zhou, Y. Liu, H. Pang, H. Zhang, D. Hao, X. Meng, P. Li, T. Kako, J. Ye, In Situ Bond Modulation of Graphitic Carbon Nitride to Construct p-n Homojunctions for Enhanced Photocatalytic Hydrogen Production, Advanced Functional Materials 26 (2016) 6822–6829.

[19] J. Zhang, M. Zhang, G. Zhang, X. Wang, Synthesis of Carbon Nitride Semiconductors in Sulfur Flux for Water Photoredox Catalysis, ACS Catal. 2 (2012) 940–948.

[20] J. Ran, T.Y. Ma, G. Gao, X.-W. Du, S.Z. Qiao, Porous P-doped graphitic carbon nitride nanosheets for synergistically enhanced visible-light photocatalytic H_2 production, Energy & Environmental Science 8 (2015) 3708–3717.

[21] H. Liu, H. Li, J. Lu, S. Zeng, M. Wang, N. Luo, S. Xu, F. Wang, Photocatalytic Cleavage of C–C Bond in Lignin Models under Visible Light on Mesoporous Graphitic Carbon Nitride through π–π Stacking Interaction, ACS Catal. 8 (2018) 4761–4771.

[22] Y. Wang, J. Yao, H. Li, D. Su, M. Antonietti, Highly selective hydrogenation of phenol and derivatives over a Pd@carbon nitride catalyst in aqueous media, J Am Chem Soc 133 (2011) 2362–2365.

[23] G. Kresse, J. Furthmüller, Efficient iterative schemes for ab initio total-energy

[24] calculations using a plane-wave basis set, Phys Rev B Condens Matter 54 (1996) 11169–11186.

[24] G. Kresse, J. Furthmüller, Efficiency of ab-initio total energy calculations for metals and semiconductors using a plane-wave basis set, Comp.mat.er.sci 6 (1996) 15–50.

[25] J.P. Perdew, K. Burke, M. Ernzerhof, Generalized Gradient Approximation Made Simple, Physical Review Letters 77 (1998) 3865–3868.

[26] G. Kresse, D. Joubert, From ultrasoft pseudopotentials to the projector augmented-wave method, Physical Review B 59 (1999) 1758–1775.

[27] K. Momma, F. Izumi, VESTA3 for three-dimensional visualization of crystal, volumetric and morphology data, Journal of Applied Crystallography 44 (2011) 1272–1276.

[28] L. Lyu, L. Zhang, G. He, H. He, C. Hu, Selective H_2O_2 conversion to hydroxyl radicals in the electron-rich area of hydroxylated C-g-C_3N_4/$CuCo$–Al_2O_3, Journal of Materials Chemistry A 5 (2017) 7153–7164.

[29] T.Y. Ma, J. Ran, S. Dai, M. Jaroniec, S.Z. Qiao, Phosphorus-doped graphitic carbon nitrides grown in situ on carbon-fiber paper: flexible and reversible oxygen electrodes, Angewandte Chemie 54 (2015) 4646–4650.

[30] Q. Liang, Z. Li, Z.-H. Huang, F. Kang, Q.-H. Yang, Holey Graphitic Carbon Nitride Nanosheets with Carbon Vacancies for Highly Improved Photocatalytic Hydrogen Production, Advanced Functional Materials 25 (2015) 6885–6892.

[31] H.-B. Fang, X.-H. Zhang, J. Wu, N. Li, Y.-Z. Zheng, X. Tao, Fragmented phosphorus-doped graphitic carbon nitride nanoflakes with broad sub-bandgap absorption for highly efficient visible-light photocatalytic hydrogen evolution, Applied Catalysis B: Environmental 225 (2018) 397–405.

[32] X. Bai, L. Wang, Y. Wang, W. Yao, Y. Zhu, Enhanced oxidation ability of g-C_3N_4 photocatalyst via C_{60} modification, Applied Catalysis B: Environmental 152–153 (2014) 262–270.

[33] L. Jiang, X. Yuan, G. Zeng, X. Chen, Z. Wu, J. Liang, J. Zhang, H. Wang, H. Wang, Phosphorus- and Sulfur-Codoped g-C_3N_4: Facile Preparation, Mechanism Insight, and Application as Efficient Photocatalyst for Tetracycline and Methyl Orange Degradation under Visible Light Irradiation, ACS Sustainable Chemistry & Engineering 5 (2017) 5831–5841.

[34] X. She, L. Liu, H. Ji, Z. Mo, Y. Li, L. Huang, D. Du, H. Xu, H. Li, Template-free synthesis of 2D porous ultrathin nonmetal-doped g-C_3N_4 nanosheets with highly efficient photocatalytic H_2 evolution from water under visible light, Applied Catalysis B: Environmental 187 (2016) 144–153.

[35] X. Ma, Y. Lv, J. Xu, Y. Liu, R. Zhang, Y. Zhu, A Strategy of Enhancing the Photoactivity of g-C_3N_4 via Doping of Nonmetal Elements: A First-Principles Study, The Journal of Physical Chemistry C 116 (2012) 23485–23493.

[36] L. Yang, J. Huang, L. Shi, L. Cao, Q. Yu, Y. Jie, J. Fei, H. Ouyang, J. Ye, A surface modification resultant thermally oxidized porous g -C_3N_4 with enhanced photocatalytic hydrogen production, Applied Catalysis B: Environmental 204 (2017) 335–345.

[37] J. Zhang, G. Zhang, X. Chen, S. Lin, L. Mohlmann, G. Dolega, G. Lipner, M. Antonietti, S. Blechert, X. Wang, Co-monomer control of carbon nitride semiconductors to optimize hydrogen evolution with visible light, Angewandte Chemie 51 (2012) 3183–3187.

[38] G-h Moon, M. Fujitsuka, S. Kim, T. Majima, X. Wang, W. Choi, Eco-Friendly Photochemical Production of H2O2 through O2 Reduction over Carbon Nitride Frameworks Incorporated with Multiple Heteroelements, ACS Catalysis 7 (2017) 2886–2895.

[39] H. Wang, B. Wang, Y. Bian, L. Dai, Enhancing Photocatalytic Activity of Graphitic Carbon Nitride by Codoping with P and C for Efficient Hydrogen Generation, ACS Appl Mater Interfaces 9 (2017) 21730–21737.

[40] J. Qin, H. Zeng, Photocatalysts fabricated by depositing plasmonic Ag nanoparticles on carbon quantum dots/graphitic carbon nitride for broad spectrum photocatalytic hydrogen generation, Applied Catalysis B: Environmental 209 (2017) 161–173.

[41] X. Zhu, J. Zhang, F. Chen, Study on visible light photocatalytic activity and mechanism of spherical $Bi_{12}TiO_{20}$ nanoparticles prepared by low-power hydrothermal method, Applied Catalysis B: Environmental 102 (2011) 316–322.

[42] R. Hou, Y. Gao, H. Zhu, G. Yang, W. Liu, Y. Huo, Z. Xie, H. Li, Coupling system of Ag/BiOBr photocatalysis and direct contact membrane distillation for complete purification of N-containing dye wastewater, Chemical Engineering Journal 317 (2017) 386–393.

[43] D. Wu, S. Yue, W. Wang, T. An, G. Li, H.Y. Yip, H. Zhao, P.K. Wong, Boron doped BiOBr nanosheets with enhanced photocatalytic inactivation of Escherichia coli, Applied Catalysis B: Environmental 192 (2016) 35–45.

[44] M.Y. Ye, Z.H. Zhao, Z.F. Hu, L.Q. Liu, H.M. Ji, Z.R. Shen, T.Y. Ma, 0D/2D Heterojunctions of Vanadate Quantum Dots/Graphitic Carbon Nitride Nanosheets for Enhanced Visible-Light-Driven Photocatalysis, Angewandte Chemie 129 (2017) 8407–8411.

Update

Applied Catalysis B: Environmental

Corrigendum

Corrigendum to "Internal electric field construction on dual oxygen group-doped carbon nitride for enhanced photodegradation of pollutants under visible light irradiation" [Appl. Catal. B: Environ. 256 (2019) 117705]

Fan Li[a,c], Muen Han[b], Yang Jin[d], Lili Zhang[a], Tong Li[b], Yaowen Gao[b], Chun Hu[b,*]

[a] Key Laboratory of Drinking Water Science and Technology, Research Center for Eco-Environmental Sciences, Chinese Academy of Sciences, Beijing, 100085, China
[b] Key Laboratory for Water Quality and Conservation of the Pearl River Delta, Ministry of Education, Institute of Environmental Research at Greater Bay, Guangzhou University, Guangzhou, 510006, China
[c] University of Chinese Academy of Sciences, Beijing, 100049, China
[d] School of Space and Environment, Beihang University, Beijing, 102206, China

The authors regret that the EPR spectra in Figure 7a and b were incorrect, which should be changed to the corrected Figure 7a and b.
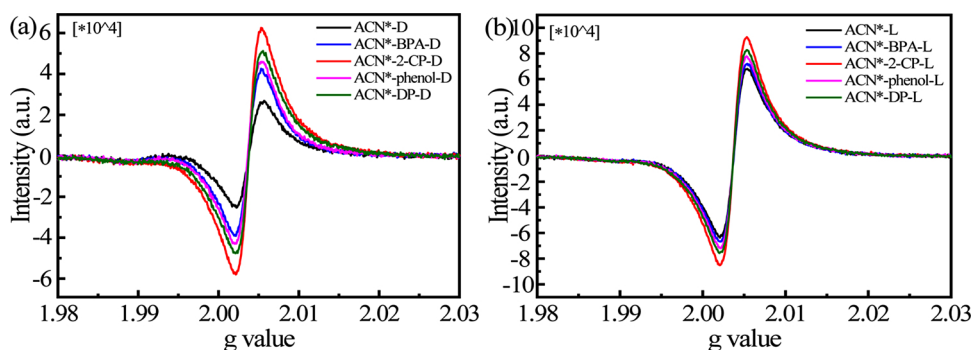
The corrections do not change the overall results and discussion and the final conclusion.
The authors would like to apologise for any inconvenience caused.

Declaration of Competing Interest

The authors declare that they have no known competing financial interests or personal relationships that could have appeared to influence the work reported in this paper.